Article

Signatures of moiré trions in WSe$_2$/MoSe$_2$ heterobilayers

Erfu Liu[1], Elyse Barré[2,3], Jeremiah van Baren[1], Matthew Wilson[1], Takashi Taniguchi[4], Kenji Watanabe[5], Yong-Tao Cui[1], Nathaniel M. Gabor[1,6], Tony F. Heinz[3,7], Yia-Chung Chang[8✉] & Chun Hung Lui[1✉]

Moiré superlattices formed by van der Waals materials can support a wide range of electronic phases, including Mott insulators[1–4], superconductors[5–10] and generalized Wigner crystals[2]. When excitons are confined by a moiré superlattice, a new class of exciton emerges, which holds promise for realizing artificial excitonic crystals and quantum optical effects[11–16]. When such moiré excitons are coupled to charge carriers, correlated states may arise. However, no experimental evidence exists for charge-coupled moiré exciton states, nor have their properties been predicted by theory. Here we report the optical signatures of trions coupled to the moiré potential in tungsten diselenide/molybdenum diselenide heterobilayers. The moiré trions show multiple sharp emission lines with a complex charge-density dependence, in stark contrast to the behaviour of conventional trions. We infer distinct contributions to the trion emission from radiative decay in which the remaining carrier resides in different moiré minibands. Variation of the trion features is observed in different devices and sample areas, indicating high sensitivity to sample inhomogeneity and variability. The observation of these trion features motivates further theoretical and experimental studies of higher-order electron correlation effects in moiré superlattices.

Two-dimensional (2D) moiré superlattices provide fertile ground to explore novel condensed-matter physics and applications. When two van der Waals materials are stacked together, the lattice mismatch and/or twist angle between them can generate a nanoscale moiré pattern, which periodically modulates the interlayer interaction (Fig. 1a). The resultant moiré superlattices can exhibit flat minibands and strong correlation effects, as demonstrated by the correlated insulating, superconducting and magnetic phases in the moiré superlattices[1–10]. With respect to optical properties, semiconducting moiré superlattices can confine excitons in moiré potential wells[11–14]. The resultant moiré excitons can show sharp emission lines[14,17,18] and distinctive valleytronic properties[14]. Such moiré excitons hold promise for novel applications, such as realizing artificial excitonic crystals and novel quantum light emitters[14–16].

To harness moiré excitons for novel applications, it is important to understand their interactions with other charge carriers. When conventional excitons interact with charge carriers, they can form charged excitons, trions or exciton–polarons. Similar phenomena are expected for moiré excitons, but their characteristics may differ from conventional behaviour due to the presence of a moiré superlattice. Moreover, as the injected carriers can fill one or more moiré minibands, the moiré system provides the opportunity to study excitons coupled to a Bloch band that can be continuously tuned from empty to fully filled. Experimental observation of charge-coupled moiré excitonic

states has, however, remained elusive. For instance, interlayer trions in transition metal dichalcogenide (TMD) heterostructures have been observed[19], but their linewidth (about 10 meV) is much broader than the expected linewidth (about 100 μeV) of moiré excitonic states[14].

Here we report several optical signatures of trions coupled to the moiré superlattice potential in tungsten diselenide (WSe$_2$)/molybdenum diselenide (MoSe$_2$) heterobilayers. First, near 1.7 eV, we see split absorption peaks of intralayer trions induced by the moiré superlattice. Second, near 1.38 eV, we resolve a series of sharp interlayer moiré trion emission lines with a complex dependence on carrier density. Third, we observe interlayer trion emission bands with different gating dependence; our theoretical simulation supports their origin as radiative recombination of trions with the remaining carriers residing in different moiré minibands. The results demonstrate substantial coupling between trions and the moiré potential and suggest trion spectroscopy as a new probe of electrons in moiré superlattices.

WSe$_2$/MoSe$_2$ heterobilayer devices

Our heterobilayers are formed by stacking monolayer WSe$_2$ and MoSe$_2$ with an approximately 0° or 60° rotation angle between the two lattices. The small difference (about 0.1%) in their lattice constants and the interlayer twist can produce a moiré superlattice with a period (L) from several to tens of nanometres (Fig. 1a). Monolayer MoSe$_2$ and WSe$_2$

[1]Department of Physics and Astronomy, University of California, Riverside, CA, USA. [2]Department of Electrical Engineering, Stanford University, Stanford, CA, USA. [3]SLAC National Accelerator Laboratory, Menlo Park, CA, USA. [4]International Center for Materials Nanoarchitectonics (WPI-MANA), National Institute for Materials Science (NIMS), Ibaraki, Japan. [5]National Institute for Materials Science (NIMS), Ibaraki, Japan. [6]Canadian Institute for Advanced Research, Toronto, Ontario, Canada. [7]Department of Applied Physics, Stanford University, Stanford, CA, USA. [8]Research Center for Applied Sciences, Academia Sinica, Taipei, Taiwan. ✉e-mail: yiachang@gate.sinica.edu.tw; joshua.lui@ucr.edu
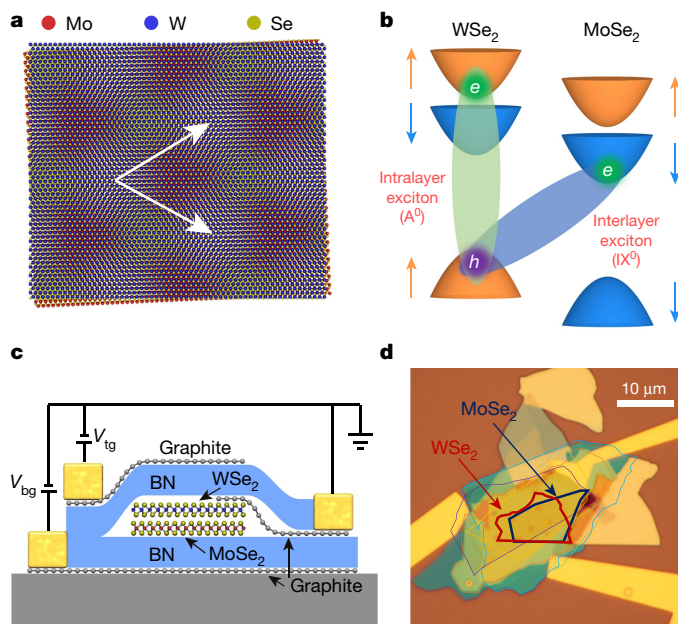
Fig. 1 | WSe₂/MoSe₂ heterobilayer with moiré superlattice. a, Illustration of the moiré pattern in a WSe₂/MoSe₂ heterobilayer with 57.5° twist angle. The white arrows are the superlattice unit vectors, whose length is the moiré period (*L*). **b**, Schematic band configuration of the intralayer and interlayer excitons studied in this paper, displaying the relevant valence and conduction bands of the two monolayers. The arrows and colour represent the electron spin. **c**, **d**, Schematic (**c**) and optical image (**d**) of a BN-encapsulated WSe₂/MoSe₂ heterobilayer device (device 1). V_{bg} and V_{tg} denote the bottom-gate voltage and top-gate voltage, respectively.

have staggered (type II) band alignment. Their heterobilayer hosts both intralayer and interlayer excitons (Fig. 1b). To investigate the coupling between these excitons and the charge carriers, we have fabricated and measured many WSe₂/MoSe₂ gated heterobilayer devices encapsulated by hexagonal boron nitride (BN) and equipped with thin graphite as electrodes. This paper focuses on the results of our best device (device 1 with a twist angle of approximately 60°); the results of additional devices are presented in Extended Data Figs. 9, 10.

Intralayer moiré excitons and trions

We first characterize the moiré superlattice by measuring the excitonic absorption spectra at varying gate voltage (V_g). Monolayer WSe₂ shows the well-known A exciton (A⁰) and trions (A⁺, A*⁻ and A⁻) around 1.7 eV. In the same spectral range, the WSe₂/MoSe₂ heterobilayer shows two A-exciton peaks (MA⁰₁,₂), two hole-side trion peaks (MA⁺₁,₂) and three electron-side trion peaks (MA⁻₁₋₃) (Extended Data Fig. 1). These split features show the strong superlattice effect on the excitonic states, in accordance with previous studies[2,3,12] and our modelling below.

We have calculated the excitonic absorption spectra to model our experimental results. We start with a lattice-matched 2H-stacked WSe₂/MoSe₂ heterobilayer and use density functional theory to calculate the band structure, charge distribution and interparticle Coulomb interactions. We adopt an effective-mass theory to describe the particle kinetic energy. We account for the moiré superlattice by a simple 2D sinusoidal potential, neglecting possible atomic reconstruction in the superlattice, and subsequently calculate the minibands for carriers, excitons and trions, as well as the optical absorption and emission spectra of excitons and trions (Methods, Supplementary Information). By using a superlattice period of *L* = 20 nm and a potential depth of *V* = 8 meV for each carrier, we can reproduce the split absorption peaks of intralayer excitons (MA⁰₁,₂) and trions (MA⁺₁,₂) (Extended Data Fig. 2).

We are uncertain about the origin of MA⁻₁₋₃, but their split features strongly suggest the effect of a moiré superlattice.

Interlayer moiré excitons

We next study the superlattice effect on the interlayer excitons and trions present at lower energies (1.37–1.40 eV). Owing to the electron–hole separation in opposite layers, these interlayer states have low oscillator strength and optical absorption, but they can emit observable luminescence owing to their large accumulated population. For an incident laser power of *P* = 3.8 µW, the heterobilayer photoluminescence (PL) spectrum is dominated by the spin-triplet interlayer exciton emission (IX⁰, 1.389 eV)[16,20–28], whereas the intralayer exciton emission (1.55–1.75 eV) is strongly suppressed because of the rapid electron–hole separation (Fig. 2a). Our interlayer exciton linewidth of 1.0 meV (Fig. 3b) compares favourably with the narrowest linewidths (≥4 meV) reported in the literature[29] and shows the high device quality. At about 25 meV above the spin-triplet interlayer exciton, we also observe the spin-singlet interlayer exciton emission, which is weak at low temperature but becomes brighter at higher temperature (Extended Data Fig. 3). These results are consistent with previous reports in WSe₂/MoSe₂ heterobilayers with a roughly 60° twist angle[30,31].

When the laser power is decreased to *P* ≈ 20 nW, the interlayer exciton peak (IX⁰) evolves into multiple discrete sharp lines (with linewidths of about 200 µeV) (Fig. 2b, Extended Data Fig. 4). We identify these fine lines as arising from interlayer moiré excitons (MX⁰), in accordance with previous studies[14,17,18]. When the interlayer exciton density is high, the repulsive exciton–exciton interaction reduces the effective modulation of the moiré potential; the excitons then approach the regime of free-particle behaviour, showing, for example, measurable diffusivity[32]. However, in the limit of low excitation density, the excitons experience the full moiré potential, becoming localized and exhibiting sharp PL features. The observed energy separation (1–4 meV) between IX⁰ and MX⁰ is comparable to the carrier well depth (*V* = 8 meV) in our model potential and the calculated well depth (about 10 meV) in previous studies[14,16], consistent with our scenario.

The MX⁰ lines are spaced by 0.3–0.7 meV and show comparable emission strengths. Such splittings do not correspond to quantized levels of confined single excitons, as our calculations indicate that such levels are more widely spaced and the ground state should dominate the emission (Extended Data Fig. 5, Methods). The MX⁰ lines also cannot be attributed to trapping at different locations within a moiré cell because theory shows only one sufficiently deep potential minimum that can trap an exciton in a moiré cell[13,33]. The multiple lines may arise from moiré cells with different numbers of trapped excitons, as the interexciton repulsion can slightly shift the emission energy of each exciton (Extended Data Fig. 6, Methods) and blueshift the whole exciton emission band at high exciton density (Extended Data Fig. 4). At low densities, the presence of multiple lines may also reflect moiré cells with slightly different potential depths due to sample inhomogeneity, as discussed later.

Interlayer moiré trions

The interlayer excitonic emission shows a striking charge-density dependence under electrostatic gating (Fig. 2). For *P* ≈ 20 µW, IX⁰ redshifts and subsides with increasing electron or hole density. A new feature IX⁻₁ (IX⁺₁) appears at about 5 meV (about 6 meV) below IX⁰ on the electron (hole) side. We attribute these features to free interlayer trions because the spacings are close to our calculated trion binding energies for IX⁺ (3.4 meV) and IX⁻ (4.9 meV) (Methods, Supplementary Information). In addition, at 4–8 meV below IX⁻₁ (IX⁺₁), we observe a weaker peak IX⁻₂ (IX⁺₂). They are not phonon replicas because the energy spacings do not match the zone-centre phonon energies. Under an out-of-plane magnetic field, IX⁰ and IX⁺₁₋ all show Zeeman splitting with nearly the
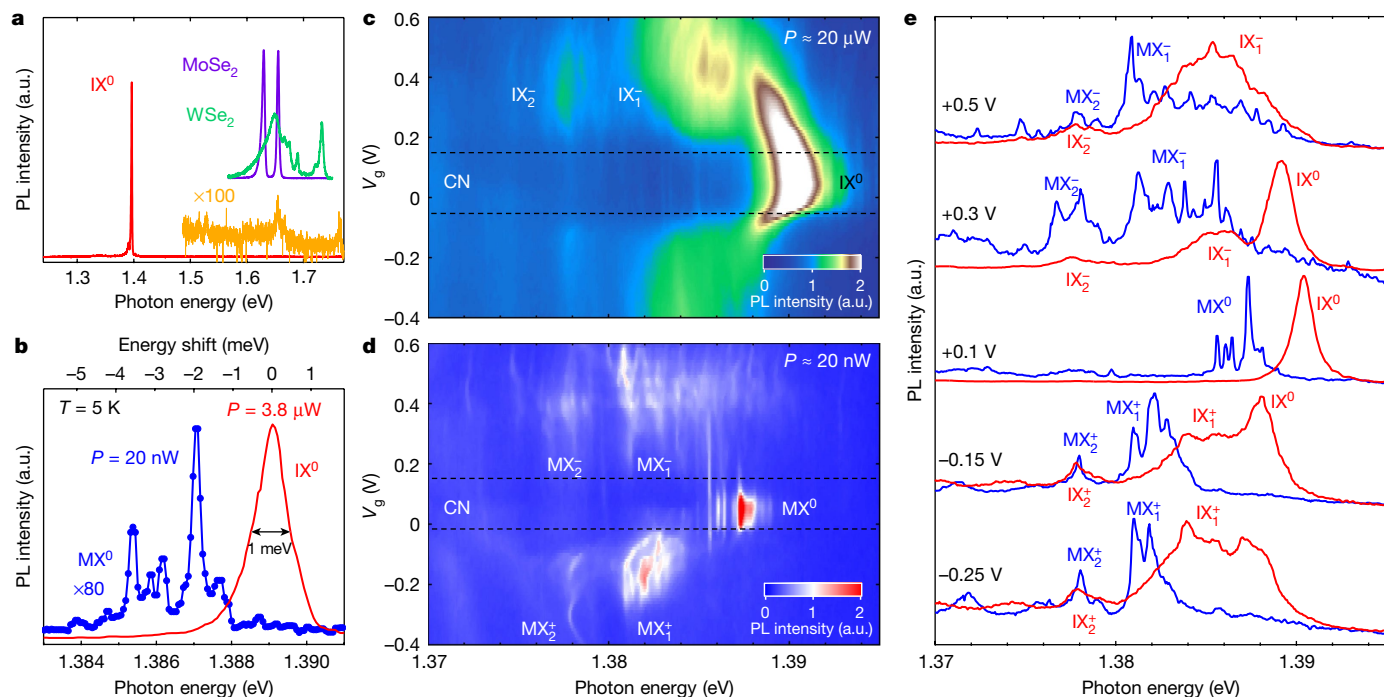
Fig. 2 | Gate-dependent PL of the WSe₂/MoSe₂ heterobilayer device. a, A PL spectrum of the WSe₂/MoSe₂ heterobilayer with the interlayer exciton peak (IX⁰) at about 1.4 eV (red line). The orange spectrum shows the intralayer exciton PL with 100-times-longer integration time. The vertically displaced purple (green) spectrum is the exciton PL of the isolated monolayer MoSe₂ (monolayer WSe₂). **b**, The PL spectra for the free interlayer exciton (IX⁰) and moiré excitons (MX⁰) at incident laser powers of $P = 3.8\,\mu W$ and $P = 20\,nW$, respectively. The linewidth is 1.0 meV (about 200 μeV) for IX⁰ (MX⁰).

c, **d**, Gate-dependent PL maps for $P = 20\,\mu W$ (**c**) and $P = 20\,nW$ (**d**). The positive (negative) gate voltage (V_g) corresponds to the electron (hole) doping. The free interlayer exciton and trion peaks (IX⁰, IX$_1^\pm$ and IX$_2^\pm$) and their associated moiré emission lines (MX⁰, MX$_1^\pm$ and MX$_2^\pm$) are indicated. CN denotes charge neutrality. **e**, The normalized PL spectra at $V_g = +0.5$, $+0.3$, $+0.1$, -0.15 and -0.25 V for $P = 20\,\mu W$ (red) and $P = 20\,nW$ (blue). The measurements were performed at sample temperature of $T \approx 5$ K and zero magnetic field under 532-nm laser excitation.

same g-factor of $g \approx 16$ (Fig. 3); this indicates that they are all associated with the spin-triplet interlayer excitonic state[14,30,34] (Extended Data Fig. 7).

When the laser power is decreased to $P \approx 20$ nW, IX$_1^\pm$ and IX$_2^\pm$ evolve into sharp, discrete lines (MX$_1^\pm$ and MX$_2^\pm$). We identify these states as interlayer trions confined by the moiré potential for the following reasons. First, their linewidth (about 200 μeV) is comparable to the moiré exciton linewidth (about 200 μeV). Second, the MX$_1^\pm$ lines are 0–7 meV below the IX$_1^\pm$ peaks, comparable to the redshift energy (1–4 meV) of MX⁰ moiré excitons from the IX⁰ free exciton. Third, MX⁰ and MX$_{1,2}^\pm$ have almost the same Zeeman splitting g-factor of $g \approx 16$, indicating that they are all associated with the spin-triplet interlayer excitonic state (Fig. 3, Extended Data Fig. 7). Finally, the trion emission shows fine, closely spaced lines, like the moiré exciton features, suggesting a similar origin.

The interlayer moiré exciton states show an interesting dependence on charge density. With increasing carrier density, the MX⁰ lines do not shift in energy, whereas IX⁰ clearly redshifts (Fig. 3c, d). This distinct gate dependence can be understood qualitatively by their different nature of exciton–carrier interaction. The IX⁰ excitons are free to move laterally; they can thus interact effectively with ambient carriers to produce an observable energy shift. But the MX⁰ excitons are confined within the moiré cells; they interact only weakly with carriers outside their own cells and hence show no appreciable energy shift.

Unlike the moiré excitons, the moiré trions exhibit a complex gate dependence. We have examined the hole-side trion PL map and found three notable features (Fig. 4a). First, the map shows two gating regions (I and II, separated by the horizontal dashed line). Second, the MX$_1^+$ emission appears in region I, but subsides in region II. Third, the MX$_2^+$ emission breaks into two segments (MX$_{2, I}^+$ and MX$_{2, II}^+$) in regions I and II. Emission with similar characteristics is also observed on the electron

and hole sides under a strong magnetic field (Fig. 3b, Extended Data Fig. 8).

To understand the origin and gating behaviour of these emission bands, we consider some key features. First, no lower-energy peak like IX$_2^\pm$ or MX$_2^\pm$ is found for neutral excitons; ambient carriers are thus needed to generate the lower-energy peaks. This also strongly suggests that the lower-energy trion peaks do not come from regions with different local lattice structure, which would affect both excitons and trions similarly. Second, the IX$_1^\pm$ – IX$_2^\pm$ and MX$_1^\pm$ – MX$_2^\pm$ energy spacings (3–8 meV) are comparable to those between the carrier minibands (Fig. 4). Third, the boundary of region I (about 0.2 V) corresponds to a carrier density of about 3×10^{11} cm^{-2}, close to the density (2.9×10^{11} cm^{-2}) needed to fill a miniband in a moiré superlattice with period $L = 20$ nm. These observations suggest a crucial role of the carrier minibands in the trion emission.

Simulation of trion emission spectra

To understand the observations above, we have calculated the trion emission spectra in the presence of a moiré potential. Our model allows an exciton to capture a carrier on the Fermi surface (with wave vector $\mathbf{k}_F$) to form a trion. The creation of a trion involves the combination of carrier states in different minibands, as the trion binding energy is comparable to the miniband spacings. Consequently, when the trion recombines radiatively, the remaining carrier can be left in different minibands (with the same $\mathbf{k}_F$ to conserve the momentum). This will produce different emission lines, with energy spacings reflecting the inter-miniband energy separation at $\mathbf{k}_F$.

Figure 4b shows our calculated trion emission spectra for 2D sinusoidal potential with $L = 13$ nm to $L = 40$ nm and $V = 8$ meV. We integrate contributions from all $\mathbf{k}_F$ states. The spectra show three noticeable
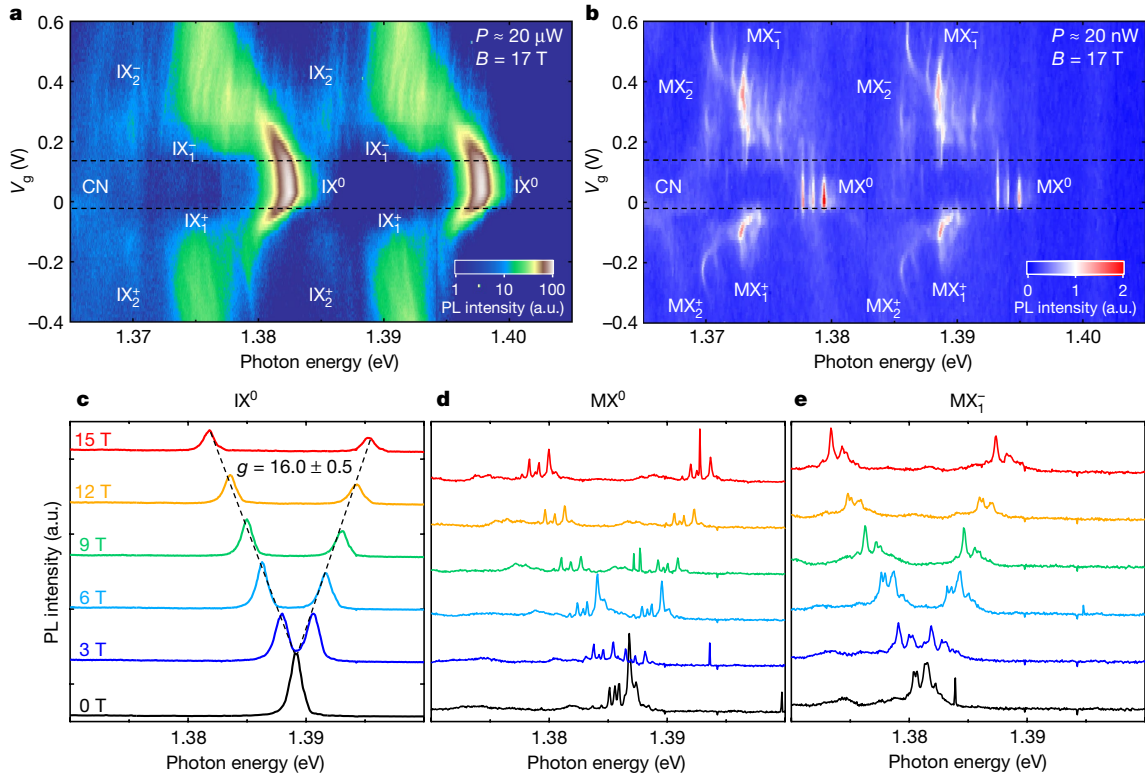
Fig. 3 | Zeeman splitting of interlayer excitonic emission in the WSe₂/MoSe₂ heterobilayer. a, b, The unpolarized PL maps for an out-of-plane magnetic field of $B = 17$ T with incident laser powers of $P = 20$ μW (**a**) and $P = 20$ nW (**b**). **c–e,** The magnetic-field dependence of the PL spectra for free interlayer

IX⁰ excitons (**c**) and moiré MX⁰ excitons (**d**) in the charge neutrality (CN) region, and of moiré trions MX₁⁻ (**e**) at $V_g = 0.5$ V. The different features show nearly the same g-factor of $g \approx 16$.

features, associated with remaining carrier states from low to high minibands. Notably, for $L = 20$ nm (the same value as in our absorption calculation), the two strongest peaks are comparable to IX₁⁺ and IX₂⁺ in relative strength and energy spacing. This supports their origin from trion decay with the remaining carrier residing in the two lowest minibands (dots in Fig. 4c).

Our model can qualitatively explain the gate-dependent behaviour of MX₁⁺ and MX₂⁺ (Fig. 4). When the carriers are injected into the first

miniband (region I), the change in $\mathbf{k}_F$ causes the trion emission energy to shift in a fashion reflecting the miniband dispersion. When the second miniband (region II) begins to be filled, state-blocking will suppress the MX₁⁺ emission, but will not impede the MX₂⁺ emission. The abrupt change of $\mathbf{k}_F$ across an indirect gap from the first to second miniband induces a discontinuity in the MX₂⁺ energy. These key features are observed in our experiment. This suggests that moiré trion spectroscopy could be a sensitive new probe of the carrier miniband structure.
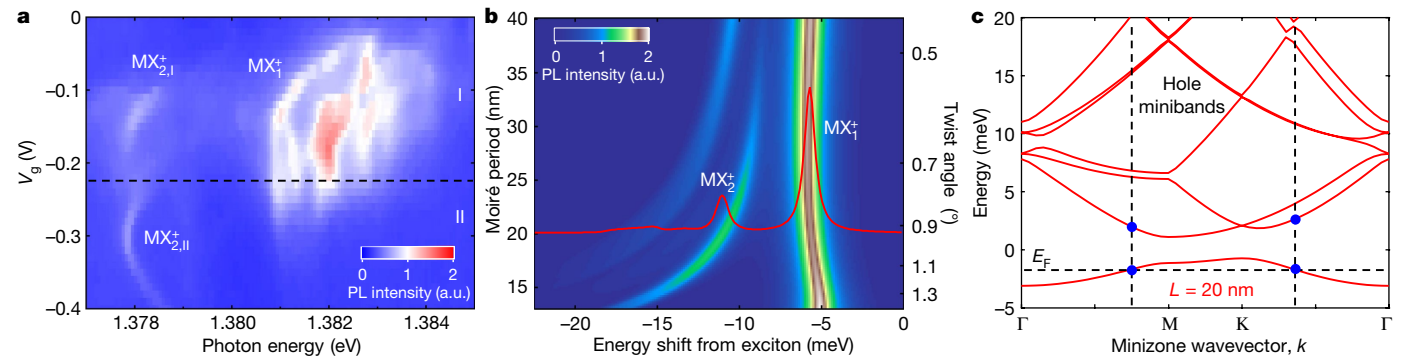
Fig. 4 | Optical signature of carrier moiré minibands in the trion emission. a, Gate-dependent PL map of the interlayer moiré trions on the hole side from Fig. 2d. The dashed line denotes the approximate full-filling position of the first hole miniband and separates the map into regions I and II. **b,** Calculated interlayer trion emission spectra (with 0.4-meV broadening) near half filling of the first hole miniband for different moiré periods (L) with $V = 8$ meV carrier potential depth. The right axis denotes the corresponding twist angle deviation from 60°. The energies of the trion spectra are offset from their

corresponding exciton energies. The red line shows the spectrum at $L = 20$ nm, in which MX₁⁺ is 5.7 meV below MX⁰ and MX₂⁺ is 5.4 meV below MX₁⁺. **c,** The calculated hole minibands in the WSe₂ layer of the heterobilayer for $L = 20$ nm and $V = 8$ meV. The minibands are plotted in the reversed energy direction. The horizontal (vertical) dashed line(s) denote the Fermi energy E_F (Fermi vectors $\mathbf{k}_F$) near half filling of the first miniband for calculating the red spectrum in **b**. The two lower (higher) blue dots denote the representative carrier final states for MX₁⁺ (MX₂⁺) after trion recombination.

Article

Sensitivity and complexity of results

The results presented above were obtained from our best device (device 1). We have also observed signatures of moiré trions in other devices with both twist angles near 0° and 60° (Extended Data Figs. 9, 10). These devices show broader PL linewidths than device 1: >3 meV (>0.3 meV) compared with about 1 meV (about 0.2 meV) at high (low) laser power. We observe variation of trion features in different devices and sample positions, to which a few factors may contribute. First, the devices are likely to have different moiré structure, as the moiré period varies sharply with twist angle near the perfect alignment due to the small (0.1%) lattice mismatch between $MoSe_2$ and WSe_2 (inset of Extended Data Fig. 5d). This variation can strongly affect the trion emission spectrum (Fig. 4b), rendering it unlikely that precisely the same features will be reproduced in different devices. Second, some degree of inhomogeneity in the distribution of charge, strain, moiré structure and lattice reconstruction is expected in our samples. Such inhomogeneity can produce broad or irregular spectral features. Further research with improved samples is merited to gain more insight.

On the theoretical side, our model does not include the influence of correlated behaviour of the injected carriers, which is known to be pronounced in some gating regimes, such as near half miniband filling[1–4]. These effects may explain abrupt changes in the trion emission features observed with gating, such as at gate voltage $V_g \approx -0.1$ V for MX_1^+ and $MX_{2,1}^\pm$ in Fig. 4a. When such strong electron correlation effects exist, the trion emission should reflect the local electron configuration, rather than the average behaviour. Moreover, the trion emission spectra are exceedingly complex on the electron side and change under a strong magnetic field (Extended Data Fig. 8). Further research that considers electron correlation and more realistic moiré potentials should help elucidate these phenomena.

Note added in proof: We became aware of two related preprints on the topic of moiré trions[35,36].

Online content

Any methods, additional references, Nature Research reporting summaries, source data, extended data, supplementary information, acknowledgements, peer review information; details of author contributions and competing interests; and statements of data and code availability are available at https://doi.org/10.1038/s41586-021-03541-z.

1. Cao, Y. et al. Correlated insulator behaviour at half-filling in magic-angle graphene superlattices. *Nature* **556**, 80–84 (2018).
2. Regan, E. C. et al. Mott and generalized Wigner crystal states in WSe₂/WS₂ moiré superlattices. *Nature* **579**, 359–363 (2020).
3. Tang, Y. et al. Simulation of Hubbard model physics in WSe₂/WS₂ moiré superlattices. *Nature* **579**, 353–358 (2020).
4. Shimazaki, Y. et al. Strongly correlated electrons and hybrid excitons in a moiré heterostructure. *Nature* **580**, 472–477 (2020).
5. Cao, Y. et al. Unconventional superconductivity in magic-angle graphene superlattices. *Nature* **556**, 43–50 (2018).
6. Bistritzer, R. & MacDonald, A. H. Moiré bands in twisted double-layer graphene. *Proc. Natl Acad. Sci. USA* **108**, 12233–12237 (2011).
7. Sharpe, A. L. et al. Emergent ferromagnetism near three-quarters filling in twisted bilayer graphene. *Science* **365**, 605–608 (2019).
8. Yankowitz, M. et al. Tuning superconductivity in twisted bilayer graphene. *Science* **363**, 1059–1064 (2019).
9. Serlin, M. et al. Intrinsic quantized anomalous Hall effect in a moiré heterostructure. *Science* **367**, 900–903 (2020).
10. Lu, X. et al. Superconductors, orbital magnets and correlated states in magic-angle bilayer graphene. *Nature* **574**, 653–657 (2019).
11. Alexeev, E. M. et al. Resonantly hybridized excitons in moiré superlattices in van der Waals heterostructures. *Nature* **567**, 81–86 (2019); correction **572**, E8 (2019).
12. Jin, C. et al. Observation of moiré excitons in WSe₂/WS₂ heterostructure superlattices. *Nature* **567**, 76–80 (2019); correction **569**, E7 (2019).
13. Tran, K. et al. Evidence for moiré excitons in van der Waals heterostructures. *Nature* **567**, 71–75 (2019).
14. Seyler, K. L. et al. Signatures of moiré-trapped valley excitons in MoSe₂/WSe₂ heterobilayers. *Nature* **567**, 66–70 (2019).
15. Wu, F., Lovorn, T. & MacDonald, A. H. Topological exciton bands in moiré heterojunctions. *Phys. Rev. Lett.* **118**, 147401 (2017).
16. Yu, H., Liu, G.-B., Tang, J., Xu, X. & Yao, W. Moiré excitons: from programmable quantum emitter arrays to spin–orbit-coupled artificial lattices. *Sci. Adv.* **3**, e1701696 (2017).
17. Baek, H. et al. Highly energy-tunable quantum light from moiré-trapped excitons. *Sci. Adv.* **6**, eaba8526 (2020).
18. Bai, Y. et al. Excitons in strain-induced one-dimensional moiré potentials at transition metal dichalcogenide heterojunctions. *Nat. Mater.* **19**, 1068–1073 (2020); correction **19**, 1124 (2020).
19. Jauregui, L. A. et al. Electrical control of interlayer exciton dynamics in atomically thin heterostructures. *Science* **366**, 870–875 (2019).
20. Rivera, P. et al. Valley-polarized exciton dynamics in a 2D semiconductor heterostructure. *Science* **351**, 688–691 (2016).
21. Rivera, P. et al. Observation of long-lived interlayer excitons in monolayer MoSe₂–WSe₂ heterostructures. *Nat. Commun.* **6**, 6242 (2015).
22. Miller, B. et al. Long-lived direct and indirect interlayer excitons in van der Waals heterostructures. *Nano Lett.* **17**, 5229–5237 (2017).
23. Yu, H., Wang, Y., Tong, Q., Xu, X. & Yao, W. Anomalous light cones and valley optical selection rules of interlayer excitons in twisted heterobilayers. *Phys. Rev. Lett.* **115**, 187002 (2015).
24. Wu, F., Lovorn, T. & MacDonald, A. H. Theory of optical absorption by interlayer excitons in transition metal dichalcogenide heterobilayers. *Phys. Rev. B* **97**, 035306 (2018).
25. Nagler, P. et al. Giant magnetic splitting inducing near-unity valley polarization in van der Waals heterostructures. *Nat. Commun.* **8**, 1551 (2017).
26. Jiang, C. Y. et al. Microsecond dark-exciton valley polarization memory in two-dimensional heterostructures. *Nat. Commun.* **9**, 753 (2018).
27. Hsu, W. T. et al. Negative circular polarization emissions from WSe₂/MoSe₂ commensurate heterobilayers. *Nat. Commun.* **9**, 1356 (2018).
28. Ciarrocchi, A. et al. Polarization switching and electrical control of interlayer excitons in two-dimensional van der Waals heterostructures. *Nat. Photon.* **13**, 131–136 (2019).
29. Calman, E. V. et al. Indirect excitons and trions in MoSe₂/WSe₂ van der Waals heterostructures. *Nano Lett.* **20**, 1869–1875 (2020).
30. Wang, T. et al. Giant valley-Zeeman splitting from spin-singlet and spin-triplet interlayer excitons in WSe₂/MoSe₂ heterostructure. *Nano Lett.* **20**, 694–700 (2020).
31. Yu, H., Liu, G.-B. & Yao, W. Brightened spin-triplet interlayer excitons and optical selection rules in van der Waals heterobilayers. *2D Mater.* **5**, 035021 (2018).
32. Wang, J. et al. Diffusivity reveals three distinct phases of interlayer excitons in MoSe₂/WSe₂ heterobilayers. *Phys. Rev. Lett.* **126**, 106804 (2021).
33. Lu, X., Li, X. & Yang, L. Modulated interlayer exciton properties in a two-dimensional moiré crystal. *Phys. Rev. B* **100**, 155416 (2019).
34. Woźniak, T., Faria, P. E. Jr, Seifert, G., Chaves, A. & Kunstmann, J. Exciton g factors of van der Waals heterostructures from first-principles calculations. *Phys. Rev. B* **101**, 235408 (2020).
35. Brotons-Gisbert, M. et al. Moiré-trapped interlayer trions in a charge-tunable WSe₂/MoSe₂ heterobilayer. Preprint at https://arxiv.org/abs/2101.07747 (2021).
36. Baek, H. et al. Optical read-out of Coulomb staircases in a moiré superlattice via trapped interlayer trions. Preprint at https://arxiv.org/abs/2102.01358 (2021).

Methods

Device fabrication

We fabricate WSe_2/$MoSe_2$ heterostructure devices with hexagonal BN encapsulation by the standard mechanical co-lamination of 2D crystals. We use WSe_2 and $MoSe_2$ bulk crystals from HQ Graphene. We first exfoliate monolayer WSe_2, monolayer $MoSe_2$, multilayer graphene and thin BN flakes from their bulk crystals onto silicon/silicon dioxide (Si/SiO_2) substrates. Afterwards, we apply a polycarbonate-based dry-transfer technique to stack these different 2D crystals together. We use a stamp to first pick up a BN flake, and sequentially pick up multilayer graphene (as the electrodes), monolayer WSe_2, monolayer $MoSe_2$, thin BN (as the bottom gate dielectric) and multilayer graphene (as the back-gate electrode). This method ensures that the WSe_2/$MoSe_2$ bilayer does not come into contact with the polymer during the fabrication process, reducing contamination and bubbles at the interface. We subsequently apply electron-beam lithography techniques to pattern and deposit the gold contacts (100-nm thickness). Finally, we anneal the devices at temperature $T = 300\ °C$ for 5 h in an argon environment to improve the interface quality. We choose $MoSe_2$ and WSe_2 monolayers, in which two sharp edges form 60° or 120° angles, and then align the sharp edges in the transfer process. The heterobilayers thus produced are expected to have twist angles near 0° or 60°. The heterobilayers with 0° (60°) twist angle exhibit constructive (destructive) interference in the optical second-harmonic generation. The second harmonic and/or g-factor measurements help us identify devices with twist angles near either 0° or 60°. The BN thickness is measured by atomic force microscopy. For device 1 highlighted in this article, the thicknesses of the top and bottom BN layers are 31 nm and 30 nm, respectively.

Reflectance contrast experiments

The reflectance contrast measurements for Extended Data Figs. 1, 9 were conducted with a closed-cycle cryostat (Montana Instruments) at UC Riverside. The sample temperature is $T \approx 15\ K$. To measure the optical reflectance, we focus broadband white light onto the sample with a spot diameter of about 2 μm using an objective lens (numerical aperture 0.6). The reflected light is collected by the same objective and analysed by a spectrometer (HRS-500-MS, Princeton Instruments) with a charge-coupled-device (CCD) camera. We measure a reflection spectrum on the sample (R_s) and a reference reflection spectrum on a nearby area without WSe_2 and $MoSe_2$ (R_r), and obtain the reflectance contrast as $\Delta R/R = (R_s - R_r)/R_r$. We further perform second-order differentiation $\Delta R/R$ with respect to photon energy to bring out the sharp features. Owing to the optical interference in the BN/TMD/BN/graphite/SiO_2/Si heterostructure, the measured reflectance contrast spectra are affected by both the real and imaginary parts of conductivity. We solve the optical problem for our stacked material system using the transfer matrix method to extract the real part of conductivity (Extended Data Fig. 1). The description of this method can be found in our previous publication[37].

PL experiments

We have performed PL experiments in different experimental setups. In all of the PL experiments, the excitation light is focused on the sample with a spot diameter of about 1–2 μm by an objective lens (numerical aperture 0.6–0.82). The PL is collected by the same objective and analysed by a spectrometer with a CCD camera. The PL data in Figs. 2–4, Extended Data Figs. 4, 8 were taken in a magneto-optical system with a 17.5-T d.c. superconducting magnet (SCM-3) at the National High Magnetic Field Laboratory in Tallahassee, Florida, USA. The sample temperature is $T \approx 5\ K$; the excitation source for PL measurements is a 532-nm continuous-wave laser; the spectrometer is IsoPlane 320 from Princeton Instruments. The PL data in Extended Data Fig. 3 (device 1) and Extended Data Fig. 10a–f (devices 2 and 3, $T \approx 5\ K$) were taken with a closed-cycle Montana cryostat, a 532-nm continuous-wave laser

(Torus 532, Laser Quantum) and a spectrometer (HRS-500-MS, Princeton Instruments) at UC Riverside. The PL data in Extended Data Fig. 10g–l (devices 4 and 5, $T = 1.7\ K$) were collected with an Attocube Attodry 2100 cryostat and a spectrometer (Shamrock 500i, Andor) equipped with a CCD camera (Newton, Andor) at Stanford University. Device 4 was excited by 730 ± 5-nm light filtered from a supercontinuum laser (FemtoPower 1060 SC540, Fianium). Device 5 was excited by a 532-nm continuous-wave laser (Verdi V5, Coherent).

For the power-dependent PL measurements in Extended Data Fig. 4, the PL shows different characteristics in three different regimes of incident laser power (P). For $P < 1\ μW$, the PL spectrum exhibits discrete sharp lines from moiré excitons, the energies of which do not change with the laser power. For $P > 2\ μW$, the PL spectrum is dominated by one peak from the free interlayer excitons. With increasing power, the peak energy blueshifts from the repulsive interactions between the interlayer excitons. As P is increased above 20 μW, the exciton peak width increases abruptly, whereas the integrated PL intensity increases only weakly with the laser power. We attribute this change to a phase transition from interlayer excitons to an interlayer electron–hole plasma[32,38].

For the temperature-dependent PL data in Extended Data Fig. 3, the spectra show two major peaks separated by about 25 meV. The lower-energy peak arises from the spin-triplet interlayer exciton and the higher-energy peak arises from the spin-singlet interlayer exciton. With increasing sample temperature, we see a shift from the emission in the lower-energy triplet states to the higher-energy singlet state. These results are consistent with previous studies of WSe_2/$MoSe_2$ heterobilayers with a 60° twist angle[30].

Zeeman effect and g-factors

The degeneracy of the K and K′ valleys in monolayer TMDs can be lifted by breaking the time-reversal symmetry with an out-of-plane magnetic field (B). The magnetic field increases the energy gap of one valley and correspondingly decreases the gap of the other valley. The difference between the gaps is the valley Zeeman splitting energy $|\Delta E| = g\mu_B B$, where μ_B is the Bohr magneton and g is the effective g-factor. Here we consider only the magnitude of the splitting energy, and thus the corresponding g-factor is positive.

In a single-particle model, the Zeeman shift of a band in monolayer WSe_2 or monolayer $MoSe_2$ can be described by[39–44]:

$$E_Z = \left(2s + m\tau + \frac{m_0}{m^*}\tau\right)\mu_B B. \tag{1}$$

Here the first term is the spin Zeeman shift, where $s = \pm1/2$ denotes the spin quantum number of the band. The second term is the atomic-orbit Zeeman shift, where τ is the valley index for the K ($\tau = +1$) and K′ ($\tau = -1$) valleys. m is the orbital magnetic quantum number in the conduction band ($m = 0$) and valence band ($m = 2$). The third term arises from the Berry-curvature contribution, with m_0 denoting the free electron mass and m^* denoting the carrier effective mass. For monolayer WSe_2, the carrier effective mass is $m^* \approx 0.42m_0$ for both the upper conduction band and the top valence band[45] and $m^* \approx 0.46m_0$ for the lower conduction band[46]. For monolayer $MoSe_2$, the carrier effective mass is $m^* \approx 0.56m_0$ for the upper conduction band, $m^* \approx 0.49m_0$ for the lower conduction band and $m^* \approx 0.59m_0$ for the top valance band[47].

On the basis of the above model and neglecting perturbations from interlayer interactions, the g-factor can be estimated for the interlayer excitons in the WSe_2/$MoSe_2$ heterobilayer with 0° and 60° twist angle. The results are shown in Extended Data Fig. 7. For the heterobilayer with 0° twist angle, the predicted g-factor is $g = 4.68$ for the spin-singlet interlayer exciton ($IX_{singlet}^0$)[48]. For the heterobilayer with a 60° twist angle, the predicted g-factor is $g = 12.34$ for the spin-singlet interlayer exciton ($IX_{singlet}^0$) and $g = 16.84$ for the spin-triplet interlayer exciton ($IX_{triplet}^0$)[30,31]. Experimentally, the Zeeman splitting energy can be measured either by the exciton PL from opposite valleys under the same magnetic field

Article

or by the exciton PL of one valley under opposite magnetic fields[39–42]. Figure 3 shows our measured PL spectra and gate-dependent PL maps under the magnetic field. The g-factor of the major PL peaks in our WSe$_2$/MoSe$_2$ heterobilayer is $g \approx 16$, which matches the predicted g-factor of IX$^0_{\text{triplet}}$ in the WSe$_2$/MoSe$_2$ heterobilayer with 60° twist angle[30].

Calculation of intralayer and interlayer excitons and trions in the WSe$_2$/MoSe$_2$ heterobilayer

Our model considers a lattice-matched 2H-stacked WSe$_2$/MoSe$_2$ heterobilayer. We first calculate the Coulomb interaction $v_{ij}(\mathbf{r}_i - \mathbf{r}_j)$ between two charge distributions averaged over the x–y plane (i, j = e, h, which denote electron and hole, respectively; $\mathbf{r}_i$ and $\mathbf{r}_j$ denote the position of electron or hole). The 2D Fourier transform of this interaction is:

$$v_{ij}(\mathbf{q}) = \frac{1}{A} \int d^2 r\, v_{ij}(\mathbf{r}) e^{i\mathbf{q}\cdot\mathbf{r}} = \frac{e^2}{2A\kappa\varepsilon_0 q} \int dz_i dz_j \rho_i(z_i) \rho_j(z_j) e^{-q|z_e - z_h|}. \quad (2)$$

Here A is the sample area; κ is the effective static dielectric constant of the BN-encapsulated sample; $\mathbf{q}$ is the wave vector; ε_0 is the vacuum permittivity; z is the out-of-plane coordinate; e is the elementary charge; $\rho_i(z_i)$ (i = e, h) denotes the normalized vertical density distribution for an electron or a hole in the WSe$_2$/MoSe$_2$ heterobilayer. The normalized density can be calculated in density functional theory via the relation $\rho_i(z_i) = \langle \psi_{i,K} | \frac{1}{c} \sum_{g_z} e^{ig_z(z - z_i)} | \psi_{i,K} \rangle$ in our 3D supercell approach. Here $\psi_{i,K}$ is the Bloch wavefunction at the K point, g_z is the z-component of the reciprocal lattice vector of the system and c is the z-axis lattice constant of the supercell.

We calculate numerically the interaction between two electrons in the MoSe$_2$ layer (v_{ee}), the interaction between two holes in the WSe$_2$ layer (v_{hh}) and the interlayer electron–hole interaction (v_{eh}) in the WSe$_2$/MoSe$_2$ heterobilayer. For reference, we also calculate the electron–hole interaction (v^W_{eh}) in monolayer WSe$_2$. Using these interactions with a dielectric constant of 4.4, which is suitable for our bilayer system, we calculate a binding energy of 152.6 meV for the intralayer exciton in the WSe$_2$ layer and 114 meV for the interlayer exciton.

For the interlayer trion calculation, we expand the trion state within a large set of basis functions and apply a variational method to estimate the trion binding energies, which are found to be 3.36 meV and 4.88 meV for the IX$^+$ and IX$^-$ interlayer trions, respectively. Note that the electron mass is about 16% heavier than the hole mass here and the calculated $v_{ee}(\mathbf{q})$ (including suitable dielectric screening) is weaker than $v_{hh}(\mathbf{q})$. This makes the binding energy for IX$^-$ larger than that for IX$^+$.

Moiré period at varying twist angle

Our above calculation of exciton and trion binding energies considers a lattice-matched WSe$_2$/MoSe$_2$ heterobilayer. In reality, between the two layers, there is a small lattice mismatch, which leads to the formation of a moiré pattern. The period of moiré pattern (L) is related to the twist angle (ϕ) by the following relation[49]:

$$L = \frac{a_<}{\sqrt{2(1+\delta)(1 - \cos\phi) + \delta^2}}, \quad \delta = 1 - \frac{a_<}{a_>} \quad (3)$$

Here $a_>$ ($a_<$) is the larger (smaller) lattice constant of the two layers. We use the lattice constant $a_< = 0.3282$ nm for WSe$_2$ and $a_> = 0.3288$ nm for MoSe$_2$, which are experimental values obtained by X-ray diffraction of the crystal power[50]. We plot the moiré period as a function of twist angle near the perfect alignment (that is, 0° or 60° twist angle) in the inset of Extended Data Fig. 5d. Owing to the small (about 0.1%) lattice mismatch between WSe$_2$ and MoS$_2$, the moiré period varies sharply from several to tens of nanometres near the perfect alignment.

Calculation of moiré exciton minibands and absorption spectra

Moiré superlattices may show a complex potential profile, including possible atomic reconstruction[51–55], which cannot be probed directly in our experiment. For simplicity, our calculations account for the influence of a moiré (M) superlattice just by adding a 2D sinusoidal potential for each carrier:

$$V_M(\mathbf{r}) = -\frac{V}{9} \sum_{j=1,6} \exp(i\mathbf{G}_j \cdot \mathbf{r}) + \frac{V}{6} - \frac{|V|}{2}. \quad (4)$$

Here $\mathbf{G}_j$ (j = 1, 2, 3 … 6) denotes the six reciprocal lattice vectors with equal magnitude and V denotes the depth of the potential well, which is assumed to be the same for an electron and a hole. A colour plot of the potential is shown as an inset in Extended Data Fig. 2c. The potential ranges from −8 meV to 0 meV.

The moiré potential profile of an exciton is taken as the sum of the potential for each constituent carrier, corrected by a form factor that accounts for the finite spatial extent of the exciton wavefunction.

Using the model exciton moiré potential, we calculate the miniband structure of intralayer moiré excitons in the WSe$_2$ monolayer of the WSe$_2$/MoSe$_2$ heterobilayer and the associated absorption spectra. By using a moiré period of $L = 20$ nm and a moiré potential depth of $V = 8$ meV for each constituent carrier, we can reproduce the split absorption peaks in our experiment (Extended Data Fig. 2a, c, e). We, therefore, attribute the splitting of exciton peak to the effect of the superlattice.

For the interlayer moiré exciton in the WSe$_2$/MoSe$_2$ heterobilayer, we calculate the exciton minibands and the associated absorption spectra for selected moiré periods of L = 10, 20, 30, 40 and 60 nm (Extended Data Fig. 5). For each L, we adjusted the potential depth (V) between 2.5 meV and 6 meV to make the ground state lie at about 4 meV below the potential maximum (0 meV) to match our observation that the lowest moiré exciton line is about 4 meV below the free-exciton peak (Fig. 2b). In our theoretical results, the two lowest absorption lines are spaced more than 2 meV apart; this is inconsistent with our observed 0.3–0.7-meV spacing in the moiré exciton lines. Therefore, the multiple moiré exciton lines are not expected to arise from the quantized levels of confined single excitons in the moiré potential wells. We also calculated the exciton absorption spectra for 2D sinusoidal potential bumps and reached the same conclusion.

Calculation of moiré trion minibands and absorption and emission spectra

Our calculation of moiré trions uses the same carrier potential ($L = 20$ nm and $V = 8$ meV) as the calculation of the intralayer moiré exciton. The trion moiré potential is the sum of the potential for each of the three particles in the trion, corrected by a form factor that accounts for the finite spatial extent of the trion wavefunction. We can reproduce the split absorption peaks for the intralayer trions in WSe$_2$ (Extended Data Fig. 2b, d, f).

We also calculate the emission spectra of the interlayer moiré trions in the WSe$_2$/MoSe$_2$ heterobilayer. We found that when an interlayer trion recombines to emit a photon, the remaining carrier (electron or hole) can be in any carrier miniband with a probability proportional to the overlap between the carrier state in the initial trion state and the final carrier state in that miniband. This leads to another prominent emission peak (IX$^\pm_2$ and MX$^\pm_2$) that is redshifted from the primary peak (IX$^\pm_1$ and MX$^\pm_1$) by an amount equal to the inter-miniband transition energy on the Fermi surface. The energy separation, relative strength and charge-density dependence of the calculated peaks are in qualitative agreement with the observed features in the experiment (Fig. 4).

Calculation of exciton–exciton repulsion energy

Two nearby interlayer excitons in the WSe$_2$/MoSe$_2$ heterobilayer repel each other because they have parallel vertical electric dipole moments[56]. Using v_{eh}, v_{ee} and v_{hh} described above, we calculated the Coulomb repulsion energy $\Delta E_{12}(R)$ between two interlayer excitons separated by a distance R (Extended Data Fig. 6). The repulsive energy

(0.7 meV) at $R = 8.8$ nm is consistent with the energy separation (about 0.7 meV) between the two lowest moiré exciton emission lines in our experiment (Fig. 2b). By using a semiclassical model, we estimated the average interexciton distance R by minimizing the total energy of two excitons inside a moiré potential well for the variation of R. We obtained an optimized value $R = 8.35$ nm for the model potential with $L = 20$ nm and $V = 8$ meV, which is close to the value $R = 8.8$ nm estimated from the 0.7-meV energy shift. The repulsion energy per exciton increases with the number of excitons in the same well. Therefore, moiré cells with a different number of excitons can emit light with slightly different photon energy.

More details of the theoretical calculations are presented in the Supplementary Information.

Data availability

The data that support the findings of this study are available from the corresponding author upon request.

37. Liu, E. et al. Landau-quantized excitonic absorption and luminescence in a monolayer valley semiconductor. *Phys. Rev. Lett.* **124**, 097401 (2020).
38. Wang, J. et al. Optical generation of high carrier densities in 2D semiconductor heterobilayers. *Sci. Adv.* **5**, eaax0145 (2019).
39. Aivazian, G. et al. Magnetic control of valley pseudospin in monolayer WSe$_2$. *Nat. Phys.* **11**, 148–152 (2015).
40. Li, Y. et al. Valley splitting and polarization by the Zeeman effect in monolayer MoSe$_2$. *Phys. Rev. Lett.* **113**, 266804 (2014).
41. MacNeill, D. et al. Breaking of valley degeneracy by magnetic field in monolayer MoSe$_2$. *Phys. Rev. Lett.* **114**, 037401 (2015).
42. Srivastava, A. et al. Valley Zeeman effect in elementary optical excitations of monolayer WSe$_2$. *Nat. Phys.* **11**, 141–147 (2015).
43. Wang, G. et al. Magneto-optics in transition metal diselenide monolayers. *2D Mater.* **2**, 034002 (2015).
44. Rostami, H. & Asgari, R. Valley Zeeman effect and spin-valley polarized conductance in monolayer MoS$_2$ in a perpendicular magnetic field. *Phys. Rev. B* **91**, 075433 (2015).
45. Nguyen, P. V. et al. Visualizing electrostatic gating effects in two-dimensional heterostructures. *Nature* **572**, 220–223 (2019).
46. Liu, E. et al. Multipath optical recombination of intervalley dark excitons and trions in monolayer WSe$_2$. *Phys. Rev. Lett.* **124**, 196802 (2020).
47. Andor, K. et al. $\mathbf{k} \cdot \mathbf{p}$ theory for two-dimensional transition metal dichalcogenide semiconductors. *2D Mater.* **2**, 022001 (2015).
48. Joe, A. Y. et al. Electrically controlled emission from singlet and triplet exciton species in atomically thin light-emitting diodes. *Phys. Rev. B* **103**, L161411 (2021).
49. Yankowitz, M. et al. Emergence of superlattice Dirac points in graphene on hexagonal boron nitride. *Nat. Phys.* **8**, 382–386 (2012).
50. Al-Hilli, A. A. & Evans, B. L. The preparation and properties of transition metal dichalcogenide single crystals. *J. Cryst. Growth* **15**, 93–101 (1972).
51. Yoo, H. et al. Atomic and electronic reconstruction at the van der Waals interface in twisted bilayer graphene. *Nat. Mater.* **18**, 448–453 (2019).
52. Weston, A. et al. Atomic reconstruction in twisted bilayers of transition metal dichalcogenides. *Nat. Nanotechnol.* **15**, 592–597 (2020).
53. Rosenberger, M. R. et al. Twist angle-dependent atomic reconstruction and moiré patterns in transition metal dichalcogenide heterostructures. *ACS Nano* **14**, 4550–4558 (2020).
54. Andersen, T. I. et al. Excitons in a reconstructed moiré potential in twisted WSe$_2$/WSe$_2$ homobilayers. *Nat. Mater.* **20**, 480–487 (2021).
55. Halbertal, D. et al. Moiré metrology of energy landscapes in van der Waals heterostructures. *Nat. Commun.* **12**, 242 (2021).
56. Li, W., Lu, X., Dubey, S., Devenica, L. & Srivastava, A. Dipolar interactions between localized interlayer excitons in van der Waals heterostructures. *Nat. Mater.* **19**, 624–629 (2020).

Author contributions E.L. fabricated the devices. E.L., E.B., J.v.B. and M.W. carried out the experiments. E.L. analysed the data. T.T. and K.W. provided boron nitride crystals for device fabrication. C.H.L., N.M.G. and Y.-T.C. supported the research of E.L. Y.-C.C. performed the theoretical calculations. T.F.H. supervised the research of E.B. and contributed to the interpretation of the data. C.H.L. supervised the research and coordinated the work. C.H.L., E.L., Y.-C.C. and T.F.H. wrote the manuscript with input from the other authors.
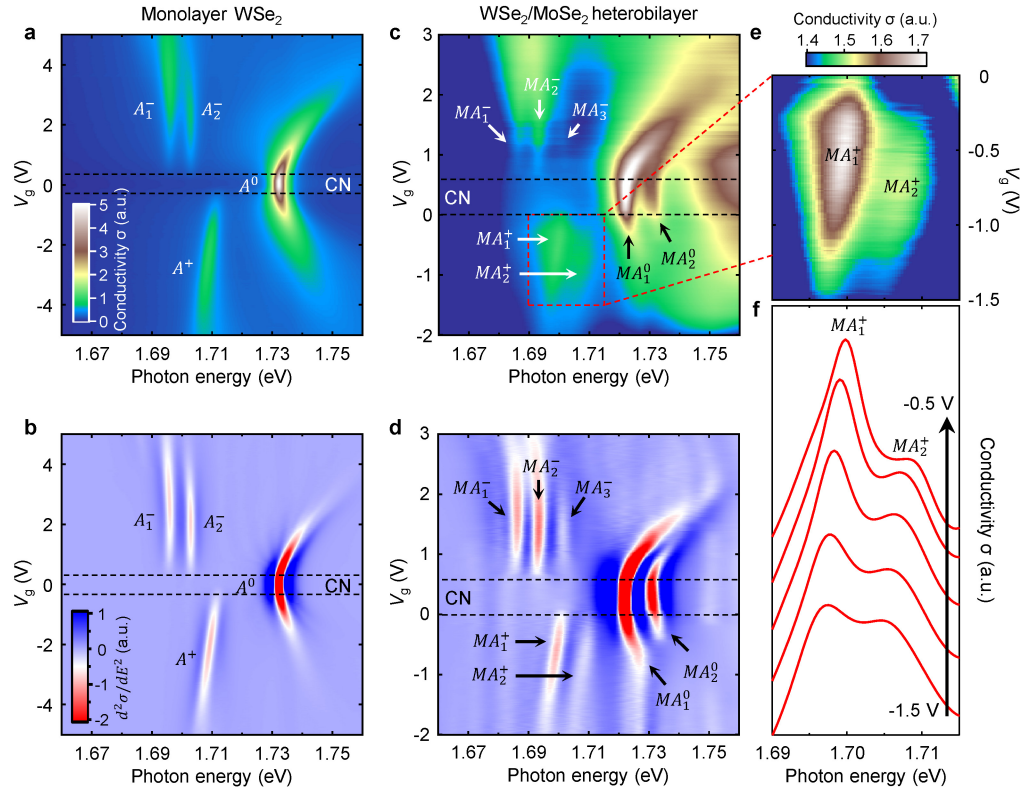
Extended Data Fig. 1 | Superlattice effect on the conductivity spectra of excitons and trions in the WSe₂/MoSe₂ heterobilayer. a, b, Gate-dependent maps of sheet conductivity, σ (**a**) and its second energy derivative, $d^2\sigma/dE^2$ (**b**) of a BN-encapsulated monolayer WSe₂ device. The A exciton (A^0) and trions (A^+ and $A^-_{1,2}$) are denoted. **c, d,** Similar maps for the WSe₂/MoSe₂ heterobilayer with a roughly 60° twist angle (device 1). The moiré A excitons ($MA^0_{1,2}$) and trions ($MA^+_{1,2}$ and MA^-_{1-3}) are denoted. The charge neutrality (CN) regions are denoted between the dashed lines. Panels **c**, **d** share the same colour scale bar with **a**, **b**, respectively. **e,** Zoom-in map of the hole-side moiré trions. **f,** Selected spectra from **e** at gate voltages from −1.5 V to 0.5 V with steps of 0.25 V. The conductivity spectra are extracted from reflectance contrast, which are measured at estimated sample temperature $T \approx 15$ K.
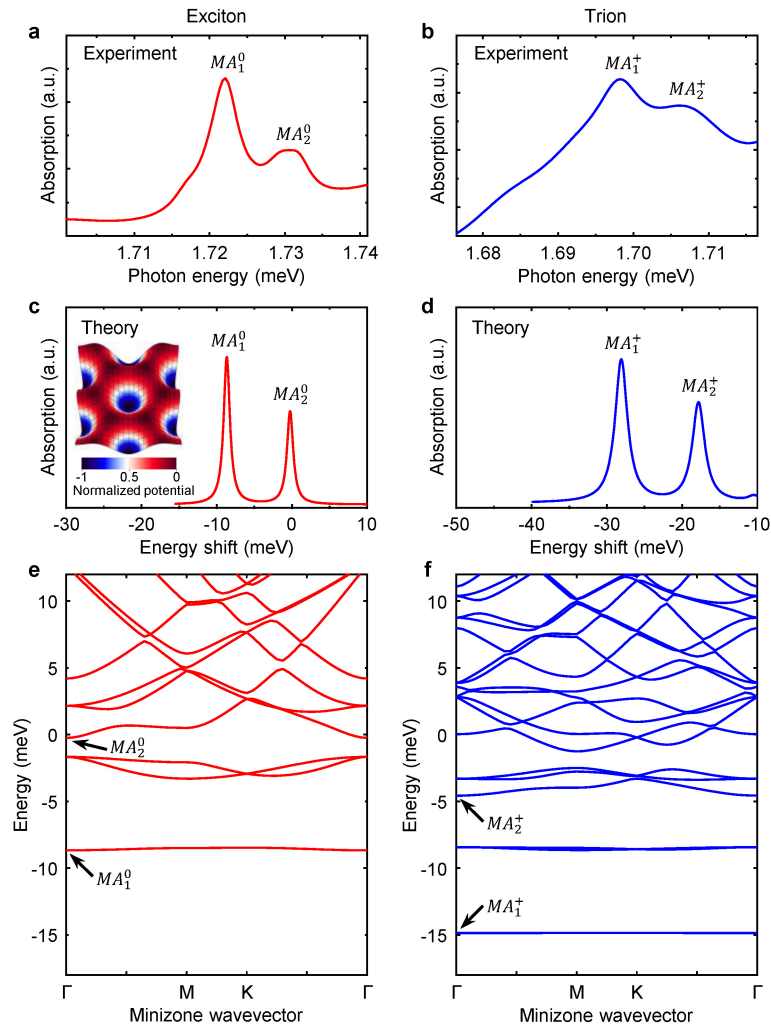
Extended Data Fig. 2 | Simulation of absorption spectra of intralayer moiré exciton and trion in the WSe₂/MoSe₂ heterobilayer. a, **b**, The experimental absorption spectra of the WSe₂ intralayer exciton (**a**) and positive trion (**b**) in the WSe₂/MoSe₂ heterobilayer. **c**, **d**, Calculated absorption spectra of intralayer moiré exciton (**c**) and trion (**d**), broadened by a Lorentzian function with half-width of 0.5 meV and 1 meV, respectively. **e**, **f**, The calculated moiré exciton (**e**) and trion (**f**) miniband structures. The corresponding states for the absorption peaks are denoted. The calculations in **c**–**f** use a 2D sinusoidal superlattice potential with period $L = 20$ nm and carrier well depth $V = 8$ meV (inset of **c**).
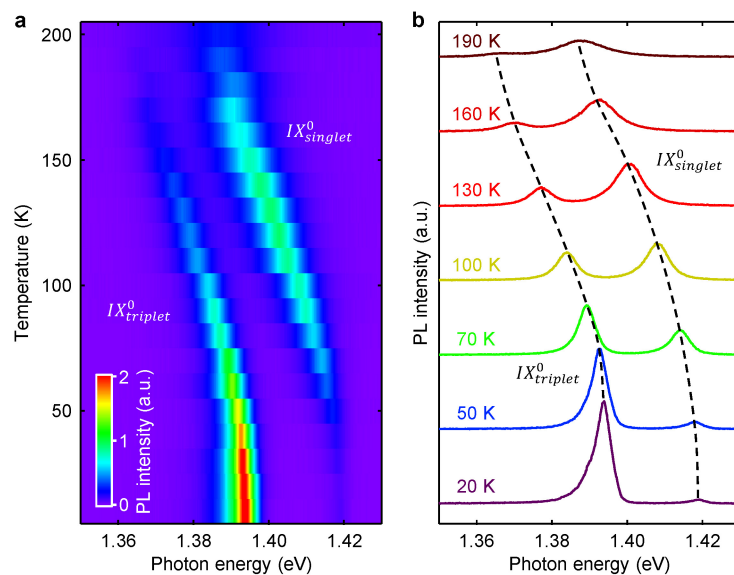
Extended Data Fig. 3 | Temperature-dependent interlayer PL in the WSe$_2$/MoSe$_2$ heterobilayer. a, Temperature-dependent PL map of the interlayer exciton. We observe both the spin-singlet and spin-triplet interlayer excitons (labelled as IX$_{singlet}^0$ and IX$_{triplet}^0$, respectively), which are separated by about 25 meV. **b**, PL spectra at selected estimated sample temperatures. The dashed lines highlight the shift of the exciton peaks.
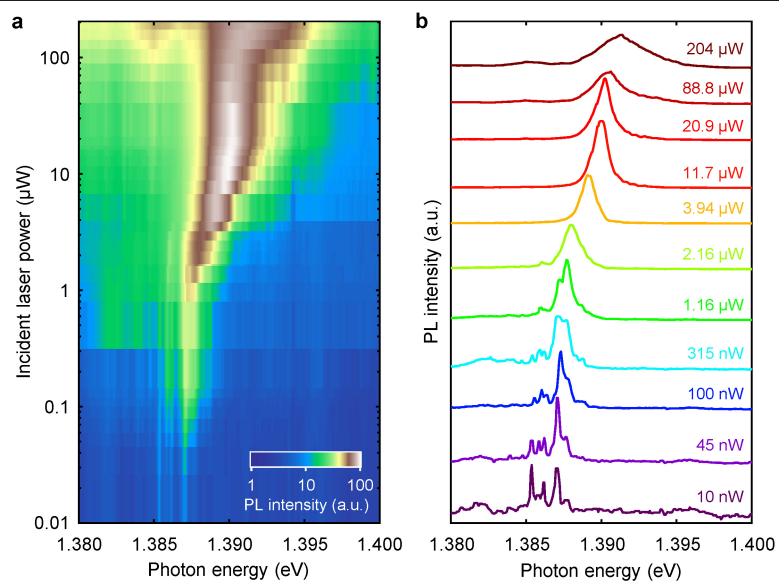
Extended Data Fig. 4 | Power-dependent interlayer PL in the WSe₂/MoSe₂ heterobilayer. a, PL map under varying incident excitation power of a 532-nm continuous laser. **b**, Normalized PL spectra at selected incident laser power. The sample temperature is $T \approx 5$ K.
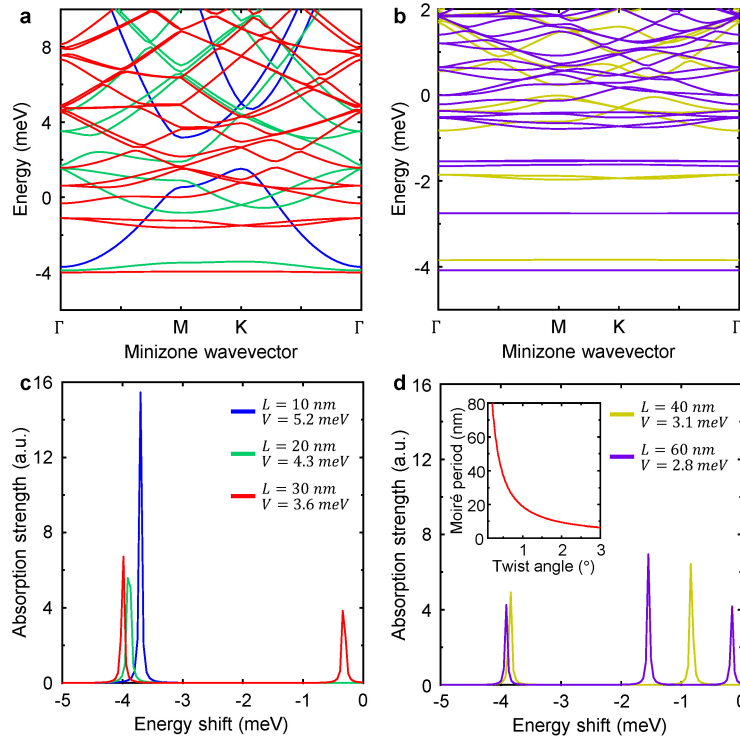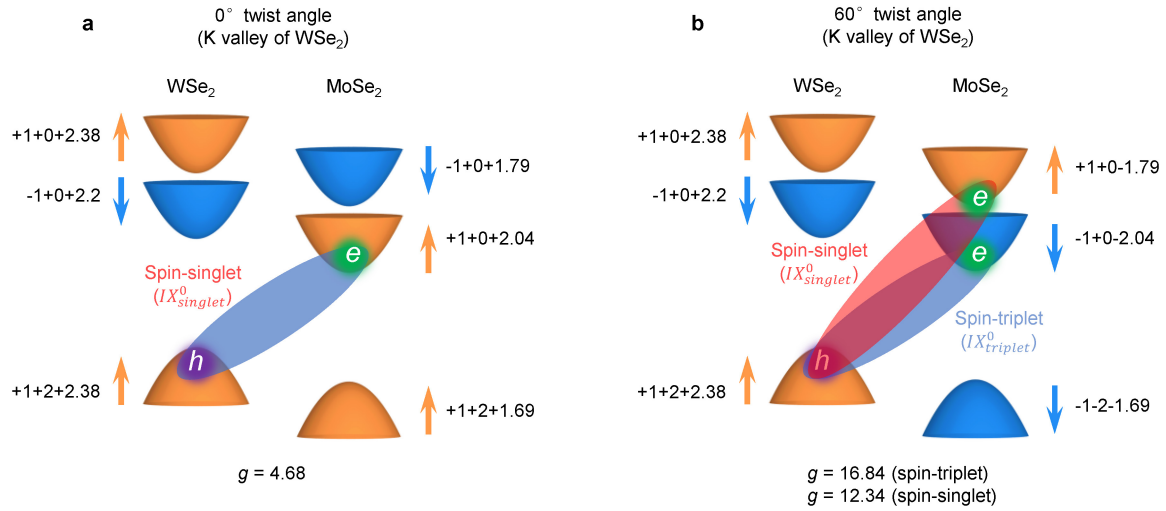
Extended Data Fig. 5 | Calculated miniband structure and absorption spectra of interlayer excitons in the moiré superlattice with 2D sinusoidal model potential. a–**d**, The calculated exciton minibands (**a**, **b**) and absorption spectra (**c**, **d**,) for superlattice periods $L = 10$, 20 and 30 nm (**a**, **c**) and $L = 40$ and 60 nm (**b**, **d**). Panels **a**, **b** share the same legends with **c**, **d**, respectively. The potential depth (V) of each carrier, denoted in **c**, **d**, is adjusted between 2.5 meV and 6 meV so that the exciton ground state lies at about 4 meV below the

potential maximum (0 meV) to match our observation that the lowest moiré exciton line is about 4 meV below the free-exciton line (Fig. 2b). Our calculations use a total exciton effective mass $m^* = 0.91m_0$, where m_0 is the free electron mass. The inset in **d** shows the calculated moiré period as a function of twist angle near the perfect alignment (that is, 0° or 60° twist angle), by using lattice constants of 0.3282 nm for the WSe_2 and 0.3288 nm for the $MoSe_2$ layer[50].
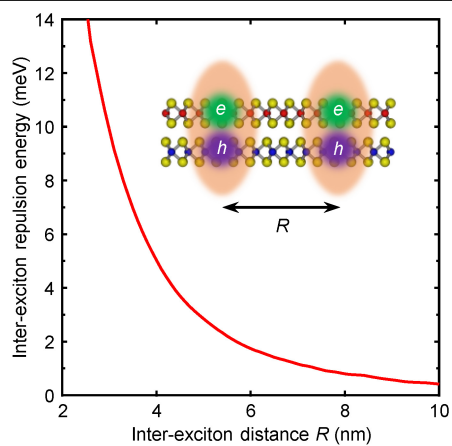
Extended Data Fig. 6 | Calculated repulsion energy between two interlayer excitons as a function of interexciton separation in the WSe$_2$/MoSe$_2$ heterobilayer. The inset illustrates two interlayer excitons in the WSe$_2$/MoSe$_2$ heterobilayer.

Article

a 0° twist angle (K valley of WSe$_2$)

WSe$_2$ MoSe$_2$

+1+0+2.38
-1+0+2.2
-1+0+1.79
+1+0+2.04
Spin-singlet ($IX^0_{singlet}$)
+1+2+2.38
+1+2+1.69

$g = 4.68$

b 60° twist angle (K valley of WSe$_2$)

WSe$_2$ MoSe$_2$

+1+0+2.38
-1+0+2.2
+1+0-1.79
-1+0-2.04
Spin-singlet ($IX^0_{singlet}$)
Spin-triplet ($IX^0_{triplet}$)
+1+2+2.38
-1-2-1.69

$g = 16.84$ (spin-triplet)
$g = 12.34$ (spin-singlet)

Extended Data Fig. 7 | Zeeman-splitting g-factors of the interlayer excitons in WSe$_2$/MoSe$_2$ heterobilayers. a, **b**, The g-factors predicted by a single-particle model for WSe$_2$/MoSe$_2$ heterobilayers with 0° (**a**) and 60° (**b**) twist angle. The Zeeman-shift g-factor of a band is contributed by the spin, atomic orbit and Berry curvature, whose component g-factor is denoted, respectively, by the first, second and third numbers near the band. The sum of these three numbers is the g-factor of the band. The Zeeman-shift g-factor of an exciton equals the difference between the g-factors of the associated conduction and valence bands. The g-factor difference between an exciton and its time-reversal partner (that is, the exciton with opposite valley configurations) is the Zeeman-splitting g-factor of the exciton. Our single-particle model predicts a Zeeman-splitting g-factor of $g = 4.68$ for the interlayer excitons in the WSe$_2$/MoSe$_2$ heterobilayer with 0° twist angle, and $g = 12.34$ and $g = 16.84$, respectively, for the spin-singlet and spin-triplet interlayer excitons in the WSe$_2$/MoSe$_2$ heterobilayer with 60° twist angle (denoted at the bottom of each panel).
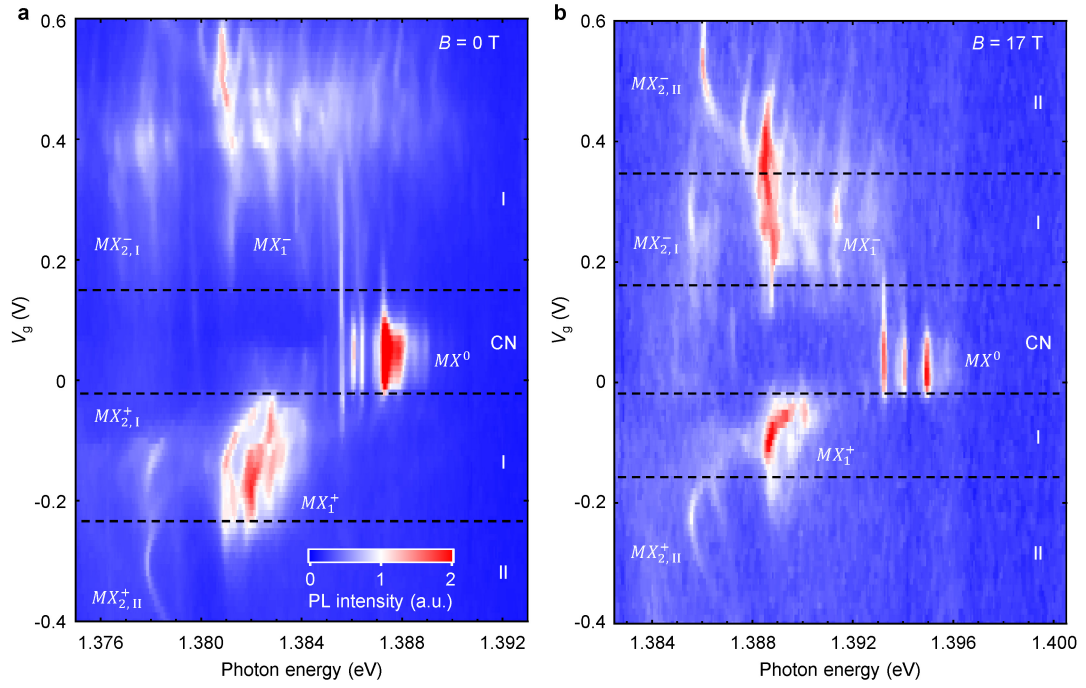
Extended Data Fig. 8 | Gate-dependent PL maps of the WSe₂/MoSe₂ heterobilayer at zero and finite magnetic field. a, The PL map at magnetic field $B = 0$ T. **b**, The PL map at $B = 17$ T. The incident laser power is $P = 20$ nW. The sample temperature is $T \approx 5$ K. Panels **a** and **b** share the same colour scale with **a**. The photon energy in **b** is higher than that in **a** due to the Zeeman shift. The dashed lines approximately highlight different charging regimes.
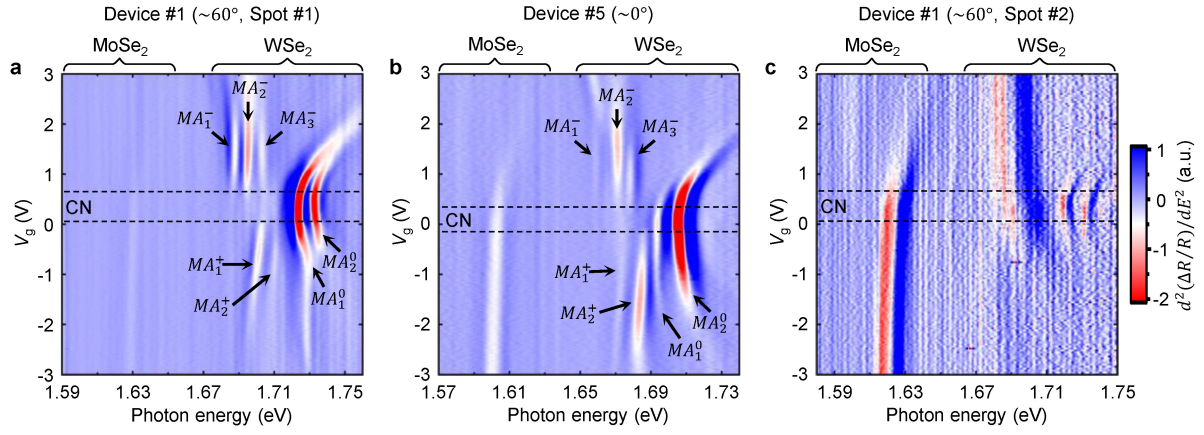
Extended Data Fig. 9 | Differential reflectance contrast maps for two different WSe₂/MoSe₂ heterobilayer devices. a, b, The gate-dependent maps of the second-order energy derivative of reflectance contrast for device 1 (**a**; twist angle of roughly 60°) and device 5 (**b**; twist angle of roughly 0°). The map in **a** corresponds to Fig. 2d. Similar split exciton and trion features are observed in both devices. However, although MA_2^+ is weaker than MA_1^+ in the roughly 60° heterobilayer, MA_2^+ is stronger than MA_1^+ in the roughly 0° heterobilayer. Moreover, the energy separation between MA_1^+ and MA_2^+ is slightly larger in the roughly 0° heterobilayer (10.7 meV) than in the roughly 60° heterobilayer (9.3 meV). These differences may be induced by the different potential depths of the roughly 0° and roughly 60° heterobilayers. **c,** A similar map at a different sample position of device 1. The variation indicates the spatial inhomogeneity of the sample. The sample temperature is estimated to be $T \approx 15$ K in these measurements.
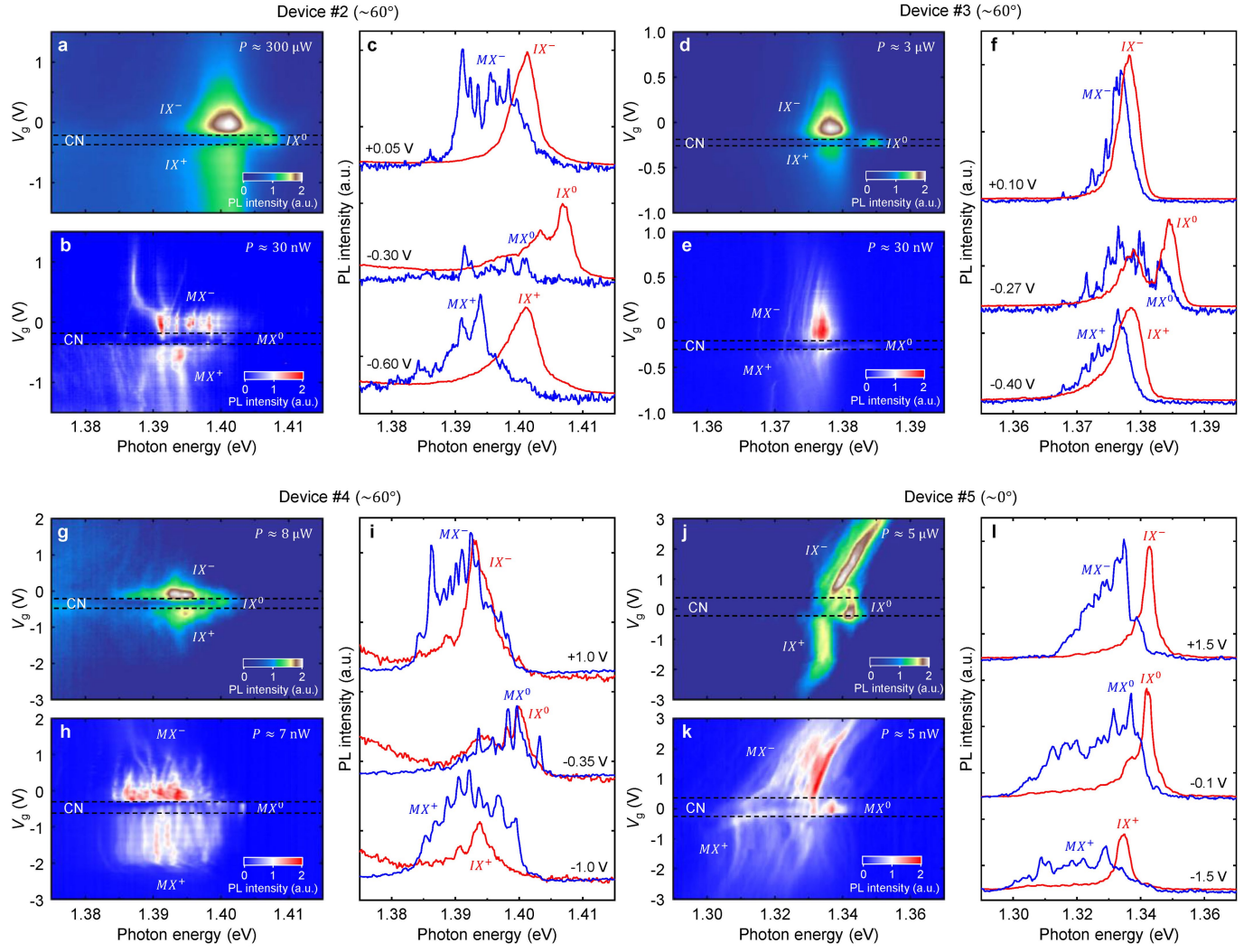
Extended Data Fig. 10 | Gate-dependent PL maps for different WSe₂/MoSe₂ heterobilayer devices. a–l, High-excitation-power PL maps (**a**, **d**, **g**, **j**), low-excitation-power PL maps (**b**, **e**, **h**, **k**) and cross-cut spectra (**c**, **f**, **i**, **l**) of device 2 (**a–c**), device 3 (**d–f**), device 4 (**g–i**) and device 5 (**j–l**). Devices 2, 3 and 4 have approximately 60° twist angles; device 5 has an approximately 0° twist angle. The panels denote the incident laser power, the free interlayer exciton and trion emission (IX⁰ and IX±) and their associated moiré exciton emission (MX⁰ and MX±). A Stark shift is observed in the interlayer trion PL of device 5 because it is a single-gate device, in which charge injection induces an interlayer electric field, whereas devices 2–4 are dual-gate devices that allow us to inject carriers without applying an electric field to the heterobilayer. Sharp trion lines are observed in all of these devices, signifying the emergence of moiré trions. The sample temperature is $T \approx 5$ K for the PL measurements of devices 2 and 3 and $T \approx 1.7$ K for the PL measurements of devices 4 and 5.